Differential equation model of an Alfvén wave maser

G. J. Morales and J. E. Maggs
Physics and Astronomy Department, University of California Los Angeles, Los Angeles, California 90095

(Received 24 February 2006; accepted 7 April 2006; published online 12 May 2006)

A mathematical model describing the operation of an Alfvén wave maser in a laboratory environment is constructed from a continuous differential equation. The model incorporates the essential features of maser operation, namely, a resonator with a semitransparent boundary, a unidirectional amplification region, and a nonuniform magnetic field that provides frequency filtering. The spectral features and the parameter scaling predicted by the model are in agreement with laboratory measurements of an Alfvén wave maser [J. E. Maggs and G. J. Morales, Phys. Rev Lett. **91**, 035004 (2003)]. The model provides a useful tool to explore a variety of operational scenarios for users of this novel wave source, including studies of Alfvénic interactions of relevance to space and fusion plasmas. © *2006 American Institute of Physics*. [DOI: 10.1063/1.2200629]

I. INTRODUCTION

It has been demonstrated in recent studies[1,2] that an Alfvén wave maser in the shear mode of polarization can be operated in the laboratory environment of the Basic Plasma Science Facility (BaPSF) at the University of California Los Angeles (UCLA). Alfvén wave masers were originally considered in theoretical studies[3,4] of magnetospheric plasmas more than 20 years ago, but suitable laboratory facilities in which to pursue the controlled investigation of the phenomena have come into operation only recently. Presently, space plasma researchers are devoting significant attention to the behavior of natural Alfvén wave resonators[5–9] formed at low altitudes by gradients in the ionospheric plasma. The interest is motivated by the possibility that such resonators can provide an environment for maser action driven by free-energy sources present in the geoplasma. The ensuing large-amplitude signals can thus play a role in auroral dynamics, as exemplified in a modeling study[10] of ion outflow from the ionosphere to fuel the magnetospheric plasma.

As noted in a review by Boswell,[11] a laboratory Alfvén wave maser provides an ideal tool to investigate a variety of questions of broad interest, ranging from space plasma topics to issues associated with alpha particles in magnetic confinement fusion. Thus, it is of interest to develop a mathematical model that allows the exploration of Alfvén maser scenarios realizable in the laboratory and which can also provide a tool for analyzing the results of future experiments. The purpose of this investigation is to develop a model based on a continuous differential equation which admits a fast numerical solution, well-suited for online exploratory studies.

The essential elements of an Alfvén wave maser are illustrated in the schematic of Fig. 1. They consist of a resonator with a partially reflecting boundary, an amplification region, and a region where the monochromatic signal propagates freely. It is in this region where a variety of studies can be performed that utilize the unique properties of the maser signal, i.e., narrow frequency band and large amplitude. An additional refinement is a filtering mechanism that reduces the number of modes that experience maser action. Since shear Alfvén waves do not propagate for frequencies ω larger than the ion-cyclotron frequency Ω_i, an effective filter results by the flaring of the confinement magnetic field on the side of the good reflecting wall of the resonator cavity. The flaring magnetic field prevents the development of an overmoded situation within the cavity.

As is explained in detail in Ref. 2, the essential ingredients illustrated in Fig. 1 are practically achieved in the plasma source region of the Large Plasma Device-Upgraded (LAPD-U) machine operating at BaPSF. The resonator cavity is the region between the cathode and the grid anode that provides the plasma source. The electron emitting cathode is the strongly reflecting element of the resonator while the grid anode, consisting of a fine wire mesh, plays the role of the partial reflector. Localized flaring of the magnetic field results from the source region being located in the last segment of the long solenoid that generates the confinement magnetic field. The amplification process arises from the return bulk-plasma current induced upon the injection of fast electrons emitted by the cathode.

The mathematical model examined here uses a second-order differential equation to describe the axial dependence of the wave magnetic field. The model includes magnetic field gradients, partially reflecting elements, unidirectional amplification, and collisional damping by both electrons and ions. The spectral features and parameter scaling predicted for the operational conditions in LAPD-U are found to be in agreement with the experimental observations. The model allows the consideration of several configurations (e.g., embedded resonators, strongly reflecting boundaries) that are the subject of ongoing experimental efforts. It also provides a tool for analyzing experiments that utilize the maser signal to study various Alfvénic interactions of relevance to space and fusion plasmas.

The paper is organized as follows. In Sec. II the elements of the mathematical model are developed. Section III proceeds to investigate numerically the predictions of the model. Section III A validates separately each physical process described by the model. Section III B examines the properties of the maser action that arise when all the elements are activated. Comparisons with experimental results

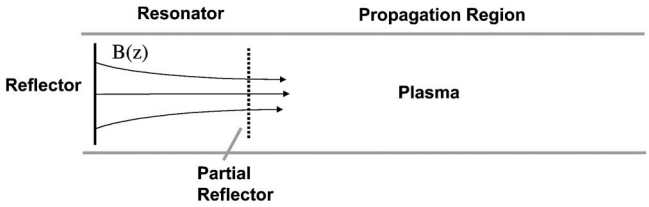

FIG. 1. Schematic of the essential elements of an Alfvén wave maser: a resonator with a partially reflecting boundary, an amplification region, and a region where the monochromatic signal propagates freely. For shear Alfvén waves a flaring of the confinement magnetic field eliminates the short wavelength modes that result in an overmoded resonator.

are established. Section III C investigates novel maser configurations associated with multiple cavities. Conclusions are presented in Sec. IV. The Appendix sketches a procedure that allows a connection between the parameters that appear in the slab formulation of Sec. II and the more realistic (but considerable more involved) cylindrical geometry.

II. ELEMENTS OF THE MATHEMATICAL MODEL

This section explains the basic elements included to model the behavior of an Alfvén wave maser operating in a laboratory environment. While the motivating reason for the model is the existing configuration in the LAPD-U, the concepts can be reasonably extended to describe other situations, perhaps including features of interest to space and astrophysical problems.

The model considers a wave in the shear mode of polarization oscillating at frequency ω, which is a real quantity. At this stage a slab description is implemented in which a real wave number $k_\perp$, transverse to the confinement magnetic field $\mathbf{B_0}$, is prescribed. The actual value of $k_\perp$ is assumed to be determined by a well-defined boundary condition in the transverse direction. In the Appendix expressions are given for how the various parameters appearing in the reduced slab formulation, including $k_\perp$, can be related to a cylindrical plasma column. The connection is achieved by performing suitable radial averages of the relevant quantities using an approximate radial wave function.

Since the key features of maser action (partial reflection, amplification, filtering) are associated with processes that break the wave symmetry along the confinement field, the desired formulation focuses on retaining axial variations, i.e., along the z direction. Thus, the final equation is a second-order differential equation that determines the z dependence of the complex amplitude of the transverse magnetic field of the wave B_y. Using a Cartesian coordinate system (x,y,z) with the z axis along $\mathbf{B_0}$, the self-consistent transverse and axial electric fields of the wave are E_x and E_z, respectively. These fields are induced by the oscillations in the magnetic field according to Faraday's law,

$$\frac{\partial}{\partial z}E_x - ik_\perp E_z = i\frac{\omega}{c}B_y, \tag{1}$$

while the magnetic fluctuations are driven by the transverse and axial plasma currents j_x and j_z according to Ampère's law,

$$\begin{aligned} ik_\perp B_y &= \frac{4\pi}{c}j_z + \frac{4\pi}{c}S, \\ \frac{\partial}{\partial z}B_y &= -\frac{4\pi}{c}j_x, \end{aligned} \tag{2}$$

in which S represents a source of fluctuations at frequency ω.

Because the maser signal is a global mode, the transverse wave number is relatively small compared to the inverse electron skin depth or the inverse ion-sound gyroradius. Thus, the more significant contribution to the wave propagation arising from the parallel electron response is represented by the resistive current given by

$$j_z = \frac{ne^2}{m\nu_{ei}}E_z, \tag{3}$$

where n is the plasma density, e is the electron charge, and ν_{ei} is the electron-ion collision frequency. This representation of the electron response is also consistent with the goal to express the model in terms of a differential equation. Inclusion of the rigorously correct kinetic electron contribution, as is necessary when describing the behavior for large values of $k_\perp$ and/or collisionless plasmas, requires an integral equation.

The wave current in the transverse direction arises from the ion-polarization drift. In this application it is necessary to retain the full frequency response (i.e., finite ω/Ω_i) as well as the scattering of the ions by the neutral atoms to properly describe this component of the current. The consideration of the broad frequency response is necessary because, *a priori*, all frequencies are candidates for partially standing modes within the resonator. The inclusion of ion-neutral collisions becomes important for frequencies close to the local ion gyrofrequency, as can be achieved by some candidate maser modes propagating along the flaring magnetic field. The inclusion of the ion-neutral collisions into the polarization current follows the self-consistent prescription validated in independent laboratory studies,[12]

$$j_x = -i\frac{\omega\omega_{pi}^2}{4\pi}\left[\frac{\xi}{\Omega_i^2 - \xi^2\omega^2}\right]E_x, \tag{4}$$

where

$$\xi = 1 + \frac{\rho_0/\rho_i}{1 - i(\rho_0\omega/\rho_i\nu_{i0})}, \tag{5}$$

with ρ_0 and ρ_i representing the mass density of the neutral atoms and the plasma ions, respectively; ν_{i0} is the ion-neutral collision frequency.

Combining Eqs. (1) through (5) results in a second-order differential equation for a shear mode of arbitrary frequency and small transverse wave number propagating through a plasma in which the confining magnetic field and the plasma density exhibit axial dependence. The wave is damped by Coulomb collisions and ion-neutral collisions. It reads

$$\frac{d}{dz}\left\{\frac{1}{\omega_{pi}^2}\left(\frac{\Omega_i^2-\xi^2\omega^2}{\xi}\right)\frac{d}{dz}B_y\right\}+\left(\frac{\omega}{c}\right)^2 \times\left[1+i\left(\frac{k_\perp c}{\omega_{pe}}\right)^2\frac{\nu_{ei}}{\omega}\right]B_y=\frac{4\pi k_\perp\omega\nu_{ei}}{c\omega_{pe}^2}S. \tag{6}$$

The next element to be incorporated into Eq. (6) is a continuum generalization of the effects produced by the semitransparent grid anode. Valuable insight into a possible mathematical representation of this component is obtained from a consideration of the scattering produced on a wave ψ, of asymptotic wave number k, by a delta-function resistive layer located at axial position z_g and having resistive strength σ. The scattering is described by a wave equation of the form

$$\frac{d^2}{dz^2}\psi+[k^2+i\sigma\delta(z-z_g)]\psi=0, \tag{7}$$

which results in the reflection and scattering coefficients having amplitudes R and T, given by

$$R=\frac{\sigma}{2k+\sigma};\quad T=\frac{2k}{2k+\sigma}. \tag{8}$$

Such a resistive layer extracts energy from the wave according to the relation

$$R^2+T^2=1-\frac{4k\sigma}{(2k+\sigma)^2}, \tag{9}$$

which indicates that maximum loss of wave power (one-half) occurs for $\sigma=2k$. However, as σ becomes much larger than $2k$ the resistive layer behaves as a good reflector and thus can play the role of a semiporous plug for the resonator. These properties approximate the subtle role of a semitransparent grid in the laboratory and, furthermore, the δ function admits a continuous generalization as the limit of a Gaussian function. Thus, a practical representation for the semitransparent anode is obtained by adding to the effective potential of Eq. (6) a grid term, $g(z)$, proportional to a Gaussian. It should be mentioned that it is also possible to model a leaky resonator by introducing a small tunneling region in the effective potential term. Upon detailed examination the resistive grid approach has been found to provide a closer representation of the experimental situation.

Expanding Eq. (6) to explicitly display the effect of the axial gradient of the plasma parameters yields

$$\frac{1}{\xi}\left(\frac{\Omega_i^2}{\omega^2}-\xi^2\right)\frac{d^2}{dz^2}B_y+\left[\frac{2\Omega_i}{\xi\omega}\frac{d}{dz}\left(\frac{\Omega_i}{\omega}\right)-\frac{1}{\xi}\left(\frac{\Omega_i^2}{\omega^2}-\xi^2\right)\frac{d}{dz}\ln(n_0)\right]\frac{d}{dz}B_y+\left(\frac{\omega_{pi}}{c}\right)^2 \times\left[1+i\left(\frac{k_\perp c}{\omega_{pe}}\right)^2\frac{\nu_{ei}}{\omega}+ig(z)\right]B_y=\frac{4\pi}{c}\left(\frac{m}{M}\right)\left(\frac{\nu_{ei}}{\omega}\right)k_\perp S, \tag{10}$$

where n_0 is the zeroth-order plasma density, and

$$g(z)=\frac{\sigma_s c}{\omega_{pi}L_g\sqrt{\pi}}\exp[-(z-z_g)^2/L_g^2], \tag{11}$$

with L_g the length scale of the grid (small compared to the wavelength), and with σ_s a normalized resistive strength, $\sigma_s=\sigma c/\omega_{pi}$, where σ is the effective resistive strength appearing in the δ-function model of Eq. (7).

Equation (10) describes the behavior of a damped shear mode that propagates through a resonator region in which the confinement magnetic field and the plasma density exhibit an axial gradient. This version of the model permits the study of driven resonances (due to the spatially dependent source S) and the filtering of those modes that match the condition $\omega=\Omega_i(z)$ at some position within the resonator.

To turn the resonator system into a maser, a region of wave amplification must be incorporated into Eq. (10). On first impression an obvious choice for the mathematical representation of such an effect would be to add an imaginary part (with suitable sign) into the effective potential term. The difficulty with such a simple scheme is that for waves that undergo multiple reflections within the resonator, the imaginary term would act as an amplifier in one direction and as a damper (of the same magnitude) in the return pass in the opposite direction. In the LAPD-U environment the amplification mechanism results from a bulk drift in the electron distribution function that cancels the current injected at the cathode by energetic, primary electrons. In this environment the amplification of the Alfvén wave is unidirectional. To describe such an effect within a second-order differential equation model it is necessary to include, in addition to the imaginary term in the effective potential, a term proportional to the first derivative. However, the coefficients of these two terms must be properly chosen to represent the desired effect of preferential amplification. The rule for linking the two coefficients can be deduced by examining a wave equation with broken symmetry such as

$$a\frac{d^2}{dz^2}\psi+b\frac{d}{dz}\psi+(\epsilon_r+i\epsilon_i)\psi=0, \tag{12}$$

where a, b, ϵ_r, ϵ_i are real constants.

Assuming a spatial dependence of the form $\exp(ikz)$, the complex propagation coefficient k can be determined analytically. In the limit of small ϵ_i, it yields the behavior of the right-going, ψ_+, and left-going, ψ_-, signals,

$$\psi_+\sim\exp(ik_rz)\exp\left[-\left(\frac{\epsilon_i}{2ak_r}+\frac{b}{2a}\right)z\right], \tag{13}$$

$$\psi_-\sim\exp(-ik_rz)\exp\left[\left(\frac{\epsilon_i}{2ak_r}-\frac{b}{2a}\right)z\right], \tag{14}$$

where $k_r=(\epsilon_r/a)^{1/2}$ and $z>0$. The requirement for unidirectional amplification is that the left-going signal should experience exponential growth (for $\epsilon_i<0$) as z decreases while the right-going signal should not be affected. This implies that the term inside the square bracket in Eq. (13) should vanish for all z, which requires that $b=-\epsilon_i/k_r$. This is the desired rule to select the coefficients that lead to maser action in the differential equation model. In its implementation the

scheme is generalized to allow the amplification region to be spatially dependent and represented by a term $\Gamma(z)$, which plays the role of ϵ_i in Eq. (12), i.e.,

$$\Gamma(z) \to \left(\frac{c}{\omega_{pi}}\right)^2 \epsilon_i. \tag{15}$$

The inclusion of a spatially dependent, unidirectional amplification region generalizes Eq. (10) to the form

$$\frac{1}{\xi}\left(\frac{\Omega_i^2}{\omega^2}-\xi^2\right)\frac{d^2}{dz^2}B_y + \left[\frac{2\Omega_i}{\xi\omega}\frac{d}{dz}\left(\frac{\Omega_i}{\omega}\right) - \frac{1}{\xi}\left(\frac{\Omega_i^2}{\omega^2}-\xi^2\right)\frac{d}{dz}\ln(n_0) - \left(\frac{\omega_{pi}}{c}\right)\Gamma(z)\left(\frac{\Omega_i^2}{\xi\omega^2}-\xi\right)^{1/2}\right]\frac{d}{dz}B_y + \left(\frac{\omega_{pi}}{c}\right)^2 \times\left[1+i\left(\frac{k_\perp c}{\omega_{pe}}\right)^2\frac{\nu_{ei}}{\omega} + ig(z) + i\Gamma(z)\right]B_y = \frac{4\pi}{c}\left(\frac{m}{M}\right) \times\left(\frac{\nu_{ei}}{\omega}\right)k_\perp S. \tag{16}$$

To preserve the symmetry of Eq. (16), we have left the coefficient of $\Gamma(z)$ in the second term complex, even though the derivation from the illustrative model, Eq. (14), assumes real coefficients.

To proceed with a numerical investigation of the predictions of the model equation, a choice must be made for the axial dependencies of the confinement magnetic field, the plasma density, the amplification region, and the source of fluctuations. In the results presented later in this paper the plasma density is taken to be uniform. This is appropriate for comparisons with the published laboratory studies,[1,2] but in the future it is possible that the effect of density nonuniformities may need to be retained. This would be particularly relevant if the large-amplitude maser fields cause nonlinear modifications in the density due to ponderomotive forces and/or plasma heating.

For simplicity and consistency of the results, the spatial dependencies of the amplification region and of the source of fluctuations are also represented by Gaussian functions, i.e.,

$$\Gamma(z) = \gamma \exp[-(z-z_a)^2/L_a^2], \tag{17}$$

$$S(z) = S_0 \exp[-(z-z_s)^2/L_s^2], \tag{18}$$

where L_a, L_s are the effective scale lengths of the amplification and source regions located at axial positions z_a, z_s, respectively. S_0 is the strength of the source of fluctuations. The magnitude of γ is the square of the ratio of the ion skin depth to the amplification e-folding length; its sign is negative to induce growth.

For laboratory applications the choice of the magnetic field variation in the resonator region is guided by the output of a magnet-design code used in the construction of the solenoid system. Of course, in geophysical applications an analogous code should be used that models the geomagnetic field. For the conditions relevant to the LAPD-U experiments, the end flaring of the confinement magnetic field near the cathode is well approximated by an exponential function of the form

$$\frac{\Omega_i(z)}{\omega} = \frac{1}{w}[1-\delta\exp(-z/L_B)], \tag{19}$$

where $z>0$, and $z=0$ corresponds to the location of the cathode. L_B is the scale length of the flaring magnetic field whose depth of variation is given by

$$\delta = \left[1-\frac{B_0(0)}{B_0(\infty)}\right], \tag{20}$$

and accordingly, $w=\omega/\Omega_i(\infty)$.

The boundary conditions used in the solution of the second-order differential equation impose perfect wave reflection at the cathode surface, i.e.,

$$\frac{dB_y}{dz} = 0 \quad \text{at } z=0, \tag{21}$$

and an outgoing wave for $z \gg z_g$. Multiple resonators can be included in the model by generalizing Eq. (11) to the form

$$g(z) = \sum_j \frac{\sigma_{sj}c}{\omega_{pi}L_{gj}\sqrt{\pi}}\exp[-(z-z_{gj})^2/L_{gj}^2]. \tag{22}$$

The multiple-resonator feature also allows the consideration of a plasma having finite axial length by choosing the value of the conductivity of a grid placed at the desired length to be very large (e.g., $\sigma_s>50$). Similar generalizations can also be considered for the source and amplification regions of Eqs. (17) and (18). With these generalizations the model permits the assessment of more complicated scenarios including frequency selectivity and standing-wave interactions.

III. NUMERICAL RESULTS

This section explores the predictions of the equation

$$\alpha(z)\frac{d^2}{dz^2}F + \beta(z)\frac{d}{dz}F + V(z)F = s(z), \tag{23}$$

describing the axial dependence of the scaled, fluctuating magnetic field of a laboratory Alfvén wave maser,

$$F(z) = \left[\frac{4\pi k_\perp \nu_{ei}}{c\omega}\left(\frac{m}{M}\right)S_0\right]^{-1}B_y(z). \tag{24}$$

The conditions examined approximate the operational environment available to users of BaPSF and dictate the evaluation of the functions

$$\alpha(z) = \frac{1}{\xi}\left[\frac{\Omega_i^2(z)}{\omega^2}-\xi^2\right], \tag{25}$$

$$\beta(z) = \frac{2}{\xi L_B}\left(\frac{\Omega_i(z)}{\omega}\right)^2\frac{\delta\exp(-z/L_B)}{1-\delta\exp(-z/L_B)} - \left(\frac{\omega_{pi}}{c}\right) \times[\alpha(z)]^{1/2}\Gamma(z), \tag{26}$$

$$V(z) = \left(\frac{\omega_{pi}}{c}\right)^2\left[1+i\left(\frac{k_\perp c}{\omega_{pe}}\right)^2\frac{\nu_{ei}}{\omega} + ig(z) + i\Gamma(z)\right], \tag{27}$$

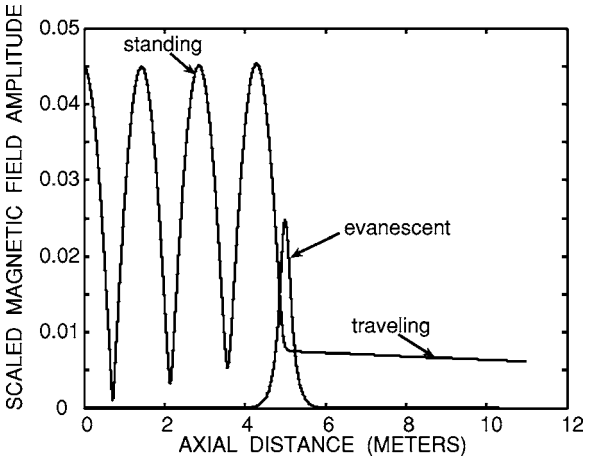

FIG. 2. Axial dependence of the magnitude of the scaled magnetic field $|F|$ for two values of the scaled frequency, $w=0.5$ (extended signal), and $w=1.2$ (evanescent signal), excited by a localized source ($L_s=0.1$ m) at $z_s=5$ m. For $z<5$ m there is a partially standing wave. For $z>5$ m a traveling wave propagates away from the source without reflection from the right-hand boundary. The localized behavior arises because the shear Alfvén mode does not propagate above the ion-cyclotron frequency.

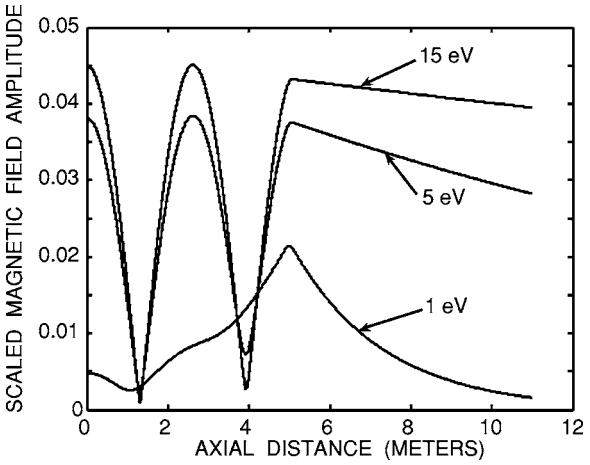

FIG. 3. Effect of electron-ion Coulomb collisions on the propagation of shear Alfvén modes excited by a localized source at $z_s=5$ m with a scaled frequency $w=0.3$. The different curves correspond to electron temperatures; $T_e=1$, 5, and 15 eV.

$$s(z) = \exp[-(z-z_s)^2/L_s^2], \tag{28}$$

in which the definitions given in Sec. II apply.

A tridiagonal numerical scheme is used to generate the results that follow. The origin of the coordinate system, $z=0$, is located at the cathode surface. For the majority of the cases reported here, nominal parameters achieved in the large plasma device (LAPD-U) operating at BaPSF are considered. The plasma density is 3×10^{12} cm^{-3}, the electron temperature is 8 eV, the ion temperature is 1 eV, the degree of ionization is 50%, the confinement magnetic field is 1 kG, and the ionic species is singly ionized helium. The typical mesh size used to properly resolve the various features of the model is $\Delta z<5\times10^{-4}$ m.

A. Propagation characteristics

The first test of the model consists of validating the propagation characteristics of the shear Alfvén mode in a uniform magnetic field and the effect on wave propagation caused by the axial boundary conditions. At this preliminary stage in the survey no grid is present and there is no amplification region. The perpendicular wave number is approximated by the expression $k_\perp=\pi/R$, with R the nominal plasma radius R=15 cm.

Figure 2 displays the axial dependence of the magnitude of the scaled magnetic field $|F|$ for two values of the scaled frequency, $w=0.5$ (extended signal), and $w=1.2$ (localized signal). The signals are excited by a localized source ($L_s=0.1$ m) placed at $z_s=5$ m. It is seen that the extended signal displays different patterns to the right and left of the source. To the left (i.e., $z<5$ m) there is an oscillatory signal. Since this represents the amplitude of the fluctuating field, this behavior implies that the signal in this region corresponds to a partially standing wave. The periodicity length corresponds to one-half of the wavelength. It is evident that in this region interference develops between the wave initially excited at the source and the right-going signal reflected at the cathode ($z=0$). The signal is not a perfect standing wave because there is dissipation present. By contrast, on the right side (i.e., $z>5$ m) the amplitude displays a monotonically decreasing pattern, which implies that no interference occurs in this region. The traveling wave on the right side of the source consists of a superposition of the right-going reflected wave and a right-going wave emitted from the source. The amplitude of the right-going traveling wave is, therefore, determined by the distance between the source and the reflector. The localized signal seen in Fig. 2 arises because the shear Alfvén mode does not propagate above the ion-cyclotron frequency (i.e., $w>1$). It is symmetric because it does not sample the reflecting boundary at the cathode.

The effect of electron-ion Coulomb collisions on the propagation of shear Alfvén modes described by the differential equation model is exhibited in Fig. 3. In this case the localized source at $z_s=5$ m launches a propagating signal with a scaled frequency $w=0.3$ (i.e., with a wavelength longer than that shown in Fig. 2). The three different curves correspond to electron temperatures $T_e=1$, 5, and 15 eV. It is found that for $T_e=1$ eV the wave is heavily damped, but it still exhibits a visible interference effect due to reflection from the cathode. As T_e is increased the electron-ion collision frequency decreases, and accordingly, the modulation of the standing wave pattern becomes deeper.

The effect of ion-neutral collisions on the signal with scaled frequency $w=0.3$ is illustrated in Fig. 4. In this case $T_e=8$ eV and $T_i=1$ eV. The four different curves show the behavior as the fractional degree of ionization is changed over the range 0.01, 0.1, 0.5, and 0.99. It is found that at the 1.0% level of ionization the shear wave does not propagate, but as the level increases to 50% the damping becomes progressively weaker. The increase from 50% to 99% ionization does not result in significant differences.

From the dependencies seen in Figs. 3 and 4 it can be concluded that the parameter space in which maser action can take place for the nominal operating environment avail-

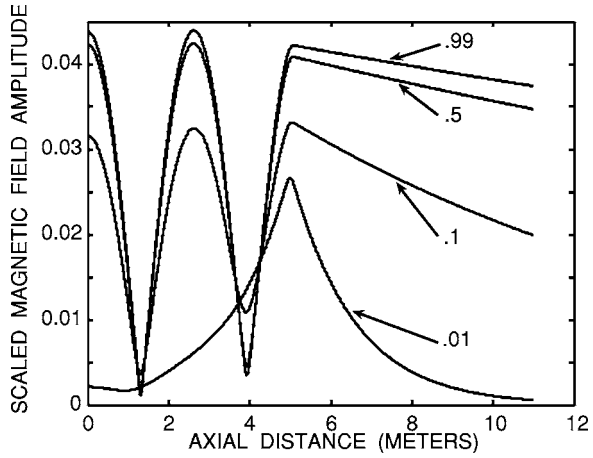

FIG. 4. Effect of ion-neutral collisions on the signal with scaled frequency $w=0.3$ in Fig. 3. In this case $T_e=8$ eV and $T_i=1$ eV. The different curves show the behavior as the fractional degree of ionization is changed over the range 0.01, 0.1, 0.5, and 0.99.

able in BaPSF requires electron temperatures of 5 eV or larger, and fractional ionization levels above 50%. Both conditions are consistent with the results of the experimental studies.[1,2]

The frequency filtering resulting from the fringing of the confinement magnetic field near the cathode ($z=0$) is demonstrated in Fig. 5. The source is located as in Figs. 2–4 and launches signals at scaled frequencies $w=0.2$ and 0.8. However, in this case a gradient in the confinement field is introduced according to the expression given in Eq. (19) with $L_B=0.25$ m and $\delta=0.35$. It is seen from Fig. 5 that the signal at $w=0.2$ behaves in a manner analogous to that of the $w=0.5$ signal for the uniform field situation considered in Fig. 2. To the left of the source ($z<5$ m) a nearly perfect standing wave is created. This demonstrates that for this lower frequency the cathode boundary behaves as a perfect

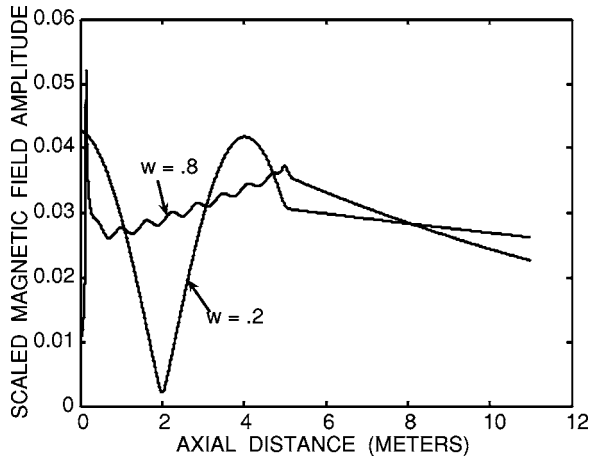

FIG. 5. Frequency filtering resulting from the fringing of the confinement magnetic field near the cathode ($z=0$). The source is located as in Figs. 2–4 and launches signals at scaled frequencies $w=0.2$ and 0.8. A gradient in the confinement field is introduced according to Eq. (19) with $L_B=0.25$ m and $\delta=0.35$. The filtering arises because the higher-frequency wave encounters a local ion-cyclotron resonance before reaching the cathode surface. The stronger damping seen for the higher-frequency mode is related to the expression given in Eq. (4).

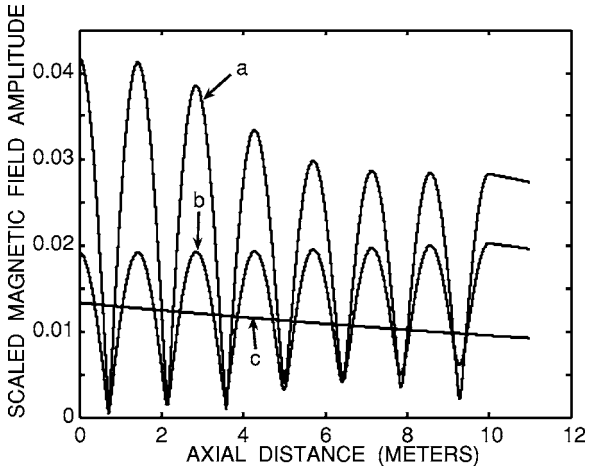

FIG. 6. Effectiveness of the unidirectional amplification scheme for a signal propagating in a uniform magnetic field with scaled frequency $w=0.5$. As in Figs. 2–5, the quantity displayed is the magnitude of the scaled magnetic field amplitude $|F|$. The curves labeled (a), (b), (c) probe the sensitivity to the direction of propagation. Curves (a) and (b) arise when the source is placed at $z_s=10$ m. Curve (b) is obtained in the absence of amplification ($\gamma=0$), while curve (a) shows the effect of an amplification region ($\gamma=-0.1$) centered at $z=4$ m with scale length $L_a=2$ m. Curve (c) actually corresponds to two overlapping curves generated with the source located at $z=0$. One of the degenerate curves is obtained with amplification present ($\gamma=-0.1$) while the other is obtained without amplification ($\gamma=0$).

reflector. However, for the $w=0.8$ wave the reflected signal is severely quenched, as indicated by the low level of modulation seen in the amplitude pattern. The filtering of the reflected signal arises because the higher frequency wave encounters a local ion-cyclotron resonance before reaching the cathode surface and thus is strongly damped. The origin of the strong damping for the higher-frequency mode is embodied in the expression given in Eq. (4). As the frequency approaches cyclotron resonance the oscillatory velocity increases and, in the presence of ion-neutral collisions, a larger amount of energy is drawn from the wave. The narrow structure seen in Fig. 5 near the cathode is the spatial shape of the wave as it approaches ion-cyclotron resonance.

The effectiveness of the unidirectional amplification scheme is illustrated in Fig. 6 for a signal with scaled frequency $w=0.5$ and propagating in a uniform magnetic field (i.e., $\delta=0$). As in Figs. 2–5, the quantity displayed is the magnitude of the scaled magnetic field amplitude $|F|$. The three curves labeled (a), (b), (c) correspond to complementary situations that probe the sensitivity to the direction of propagation. The behavior in curves (a) and (b) arises when the localized source ($L_s=0.05$ m) is placed at $z_s=10$ m , i.e., on the far-right-hand side of the figure. Curve (b) is obtained in the absence of amplification ($\gamma=0$), while curve (a) shows the effect of an amplification region ($\gamma=-0.1$) centered at $z=4$ m with scale length $L_a=2$ m, i.e., to the left of the source. Upon comparing curves (a) and (b) is it evident that signal (a) experiences net spatial amplification upon traversal of the amplification region in opposing directions, as is manifested by the formation of partially standing waves. The net-amplification feature is made clearer by the much larger signal obtained to the right of the source (i.e., $z>10$ m). The trace labeled (c) in Fig. 6 actually corresponds to two over-

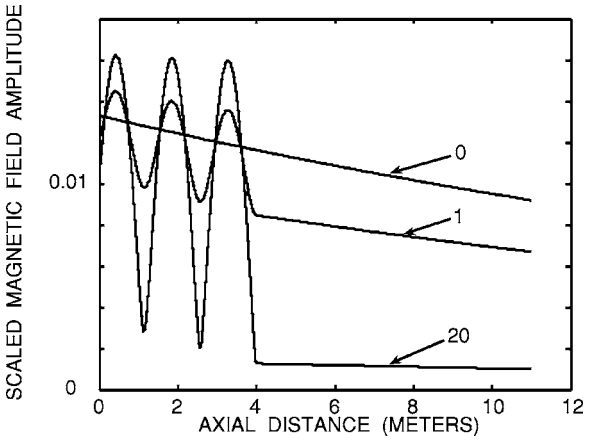

FIG. 7. Effect of the semitransparent grid for a signal with $w=0.5$. A localized ($L_s=0.05$ m) wave source is located at $z=0$ and a thin grid ($L_g=0.01$ m) is placed at $z_g=4$ m. The scaled effective conductivity is varied over the range $\sigma_s=0,1,20$ to generate the different curves. In the absence of a grid (i.e., $\sigma_s=0$) the signal exhibits a monotonic spatial dependence.

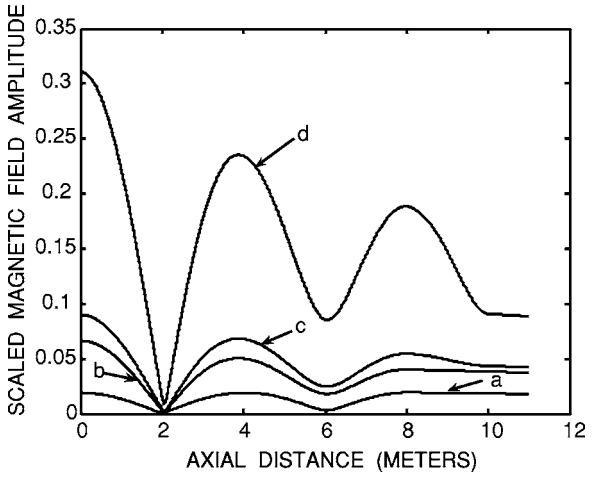

FIG. 8. Sensitivity of maser action to the value of the effective conductivity of the grid, σ_s, for a scaled wave frequency $w=0.2$. A large resonator region is considered with the grid located at $z_g=10$ m. A unidirectional amplification region is located at $z_a=4$ m with $L_a=2$ m. A localized source is placed at $z_s=8$ m. Curves (a) and (b) correspond to a case without a grid ($\sigma_s=0$) and, for (a), the absence of amplification ($\gamma=0$), and for (b) amplification with $\gamma=-0.45$. A single pass through the amplification region results in a larger signal propagating to the right of the source ($z>10$ m). Curve (c) shows the onset of maser action obtained when a resonator is present ($\sigma_s=1$). The effectiveness of multipass amplification is improved by increasing the effective conductivity of the grid as illustrated by curve (d) for $\sigma_s=5$.

lapping curves. Both of these curves are generated with the source located at the far-left-hand boundary ($z=0$); thus, the signals generated propagate along one direction (to the right), as corroborated by the absence of standing-wave oscillations. One of the degenerate curves is obtained with amplification present($\gamma=-0.1$), while the other is obtained without amplification ($\gamma=0$). The degeneracy of the result conclusively demonstrates that the right-going signals are not affected by the presence of the amplification region.

Figure 7 examines the effect of the semitransparent grid for a signal with $w=0.5$. For this purpose a localized ($L_s=0.05$ m) wave source is located at $z=0$ and a thin grid ($L_g=0.01$ m) is placed at $z_g=4$ m. The value of the scaled effective conductivity is varied over the range $\sigma_s=0$, 1, 20 to generate the three different curves shown. In the absence of a grid (i.e., $\sigma_s=0$) the signal exhibits a monotonic spatial dependence. This represents a right-going wave that experiences weak damping. For $\sigma_s=1$ it is seen that to the right of the grid (i.e., $z>4$ m) an analogous monotonic signal is present but its amplitude is reduced by about 30%. To the left of the grid (i.e., $z<4$ m) a partially standing wave is generated whose depth of modulation indicates that the grid induces a reflection close to 30%. For $\sigma_s=20$ the same features are present, but now the transmitted signal is reduced by about 90% and the depth of modulation of the partially standing wave increases by an equivalent factor. Decreasing the width of the grid by a factor of 10, i.e., to $L_g=0.001$ m, is found not to cause any visible changes in the results shown in Fig. 7.

B. Maser action

Having confirmed that each element of the differential equation model provides an adequate representation of the ingredients that are needed for an Alfvén wave maser, this section proceeds to explore the properties of the maser action that results when all the features are activated in Eq. (23).

The first feature examined is the sensitivity of maser action to the value of the effective conductivity of the grid, σ_s, for a fixed wave frequency. To better display the various features, a large resonator region is considered in which the semitransparent grid is located at $z_g=10$ m with $L_g=0.005$ m. Given the extended length of the resonator, the behavior of a nonresonant mode having relatively long wavelength is considered, i.e., $w=0.2$. The magnetic field is taken to be uniform because the frequency-filtering feature is not being tested at this stage. For clarity, the unidirectional amplification region is located near the middle of the resonator with $z_a=4$ m and $L_a=2$ m. A localized source is placed between the grid and the amplification region, i.e, at $z_s=8$ m with $L_s=0.05$ m.

Figure 8 displays the axial dependence of the scaled magnetic field for various situations represented by the curves (a), (b), (c), (d). The smallest signal represented by curve (a) corresponds to a case without a grid ($\sigma_s=0$) and in the absence of amplification ($\gamma=0$). This signal is the equivalent of the pattern displayed previously in Fig. 2 for $w=0.5$. The effect of the amplification region on this signal is illustrated by curve (b) for $\gamma=-0.45$. It is seen that the single pass through the amplification region results in a larger signal propagating to the right of the source ($z>10$ m). Curve (c) shows the onset of maser action obtained when a resonator is present (i.e., $\sigma_s=1$). The multiple passes through the amplification region provided by reflections from the grid now enhance the signal. However, the amplitude enhancement seen in curve (c) is rather modest due to the relatively low level of reflection experienced for $\sigma_s=1$ by a signal whose frequency does not correspond to a cavity resonance. The effectiveness of multipass amplification is improved by increasing the effective conductivity of the grid. This enhanced maser action is illustrated by the larger signal of curve (d) obtained for $\sigma_s=5$.

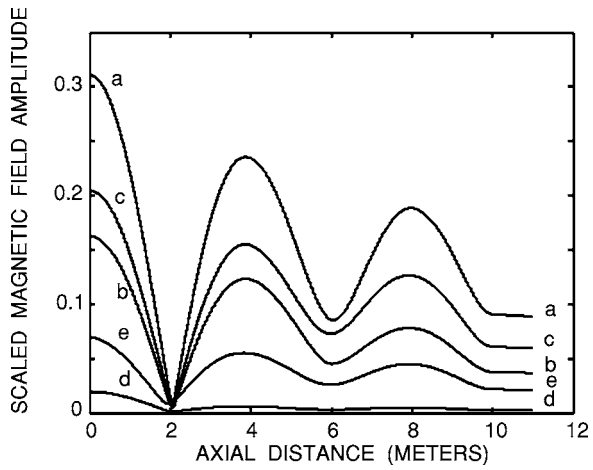

FIG. 9. Dependence of the maser signal on location of the source. The curves (a), (b), (c), (d), (e) are obtained for the same conditions used in generating the largest signal of Fig. 8 for several values of the source location, z_s. Curve (a) corresponds to $z_s=8$ m; it is identical to curve (d) of Fig. 8. The sequence (b), (c), (d), (e) is obtained by decreasing z_s progressively to the nearest maximum or minimum of the amplitude pattern of curve (a), e.g., curve (b) is driven at a minimum while (c) is driven at a maximum. The larger signals are obtained for sources located at the maximum, while smaller amplitudes result from driving at the minimum.

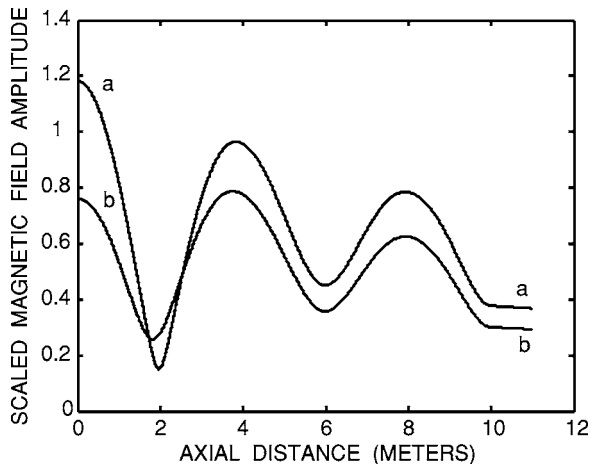

FIG. 10. Example of nonmonotonic dependence of the amplitude of maser action on the scale length of the source. Conditions correspond to those of the largest signal in Fig. 8, curve (d). Now, an extended source is applied within the 10 m long resonator, instead of the localized exciter used in generating curve (d) of Fig. 8. Curve (a) is obtained with $z_s=0$ and $L_s=1$ m, while curve (b) is the result for $z_s=0$ and $L_s=3$ m. The reason for the poorer coupling is the destructive interference within the resonator.

The dependence of the amplitude of the maser signal on the location of the source is explored in Fig. 9. All the curves (a), (b), (c), (d), (e) are obtained for the same conditions used in generating the largest signal of Fig. 8, but what is varied now is z_s, the source location. Curve (a) corresponds to $z_s=8$ m, i.e., it is identical to curve (d) of Fig. 8. The sequence of curves (b), (c), (d), (e) is obtained by decreasing z_s progressively to the nearest maxima or minima of the amplitude pattern shown by curve (a), e.g., curve (b) is driven at a minimum while (c) is driven at a maximum. It is found from the sequence of curves that the larger signals are obtained for sources located at the maxima while smaller amplitudes result from driving at the minima. The smallest maser signal in the sequence, curve (d), is obtained when the source is located at the near null close to $z=2$ m. The consequence of this behavior is that maser action preferentially amplifies background noise generated near the standing wave peaks in the resonator region.

An example of the nonmonotonic dependence of the amplitude of maser action on the scale length of an extended source is illustrated in Fig. 10. In this survey the conditions correspond to those of the largest signal shown in Fig. 8 except for the source location. Now, an extended source is applied within the 10 m long resonator, instead of the localized exciter used in generating curve (d) of Fig. 8. Curve (a) in Fig. 10 is obtained with $z_s=0$ and $L_s=1$ m, while curve (b) is the result for $z_s=0$ and $L_s=3$ m. Despite the source for case (b) being more extended within the resonator, it is not as effective as that of case (a) in exciting the $w=0.5$ signal. The reason for the poorer coupling is associated with the destructive interference between the source and a mode that exhibits spatial oscillations within the resonator. This effect is similar to the one determining the amplitude of the traveling wave to the right of the source in Fig. 2. A similar behavior results also for the location and extent of the amplification region but it is not documented here.

Having illustrated the dependencies of maser action for a nonresonant mode in a large resonator, it is appropriate to examine the spectral features of the maser action that results in a configuration corresponding to that used in the reported experimental studies.[1,2] In such a case the enhancement experienced by a resonant mode is evident, as is seen in Fig. 11.

Figure 11 displays the frequency spectrum of magnetic fluctuations (natural log of spectral amplitude) for conditions

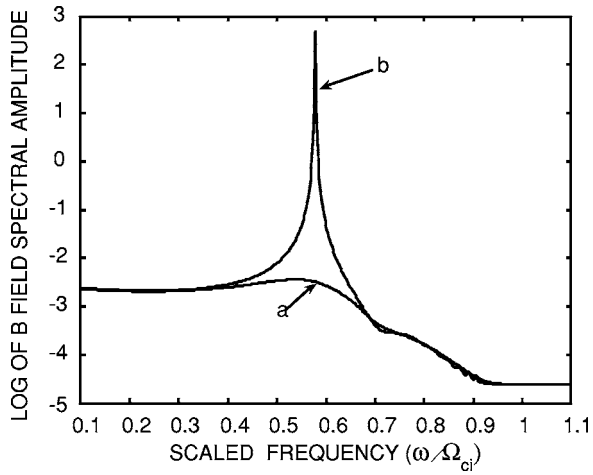

FIG. 11. Frequency spectrum of magnetic fluctuations (natural log of spectral amplitude) sampled at $z=2$ m for conditions below (a) and above (b) maser threshold. The grid location, $z_g=0.57$ m, corresponds to that of the grid anode in the LAPD-U. The effective conductivity is $\sigma_s=1.1$. A white-noise source is activated inside the resonator region. Curve (a) is obtained for $\gamma=0$. It represents the ambient noise spectrum emanating from the resonator region. The small and broad peak observed near $w=0.6$ for this case is indicative of the lowest frequency resonant mode supported by the resonator.

below (a), and above (b), maser threshold. The signal is sampled at $z=2$ m, which is located in the propagation region for waves emanating through the semitransparent grid ($z>z_g$). The grid location, $z_g=0.57$ m, corresponds to that of the grid anode in the LAPD-U. The effective conductivity is $\sigma_s=1.1$. A white-noise source is activated inside the resonator region. This choice for the source location is consistent with measurements made[13] in the LAPD-U of the properties of spontaneous Alfvénic fluctuations for conditions below maser threshold (i.e, when the plasma current leads to drift velocities smaller than the Alfvén speed). The strength of the magnetic field in the uniform region is 1 kG. The flaring at the cathode is described by Eq. (19) with $\delta=0.35$ and scale length $L_B=0.35$ m, as is appropriate for the end coil in the LAPD-U. The display in Fig. 11 scales the wave frequency to the value of the ion-cyclotron frequency in the uniform region where the signal is sampled.

Curve (a) in Fig. 11 is obtained for $\gamma=0$. It represents the ambient noise spectrum emanating from the resonator region. The small and broad peak observed near $w=0.6$ for this case is indicative of the lowest resonant mode supported by the resonator. The modes with smaller frequency are nonresonant modes having larger wavelength than the lowest resonant mode. It is seen in Fig. 11 that for $w>0.7$ the spectral amplitude is relatively small and decreases rapidly with increasing frequency. This results from two effects. One is that these modes have progressively shorter wavelengths and thus exhibit multiple spatial oscillations within the resonator. Consequently, they couple poorly to the noise source ($z_s=0.1$, $L_s=0.2$), as in the study leading to Fig. 10. The other effect is that these modes encounter a cyclotron resonance within the resonator, as illustrated by the $w=0.8$ signal in Fig. 5, and this leads to strong wave absorption. The shape of the resonator spectrum given by curve (a) is found to agree with the experimental study of spontaneous magnetic fluctuations in LAPD-U, as reported in Fig. 4 of Ref. 2, and Fig. 9 of Ref. 13.

The above-threshold behavior of the Alfvén wave maser is represented by curve (b) in Fig. 11. The operational conditions are the same as in curve (a) with the exception that an amplification region is now activated with $\gamma=-0.55$, $z_a=0$, and $L_a=3$ m (i.e., extending throughout the resonator). It is seen that the inclusion of a source of free energy selectively causes the modest peak in the noise spectrum represented by curve (a) to evolve into a sharp and large-amplitude signal. Using high numerical resolution it is found that this peak occurs at a scaled frequency $w=0.5783$. This value is determined primarily by the ratio of the length of the resonator to the ion-skin depth and is insensitive to variations in the strength of the confinement magnetic field. The predicted frequency of the maser mode is in agreement with the experimental observations reported in Refs. 1 and 2. In the experiments the scaled frequency of the maser peak ranges over $w=0.57$ to 0.65 and its width is determined by the temporal length of the plasma discharge. It should be emphasized that, while the scaled frequency is independent of magnetic field strength, the actual numerical value of the frequency of the maser signal is determined by the strength

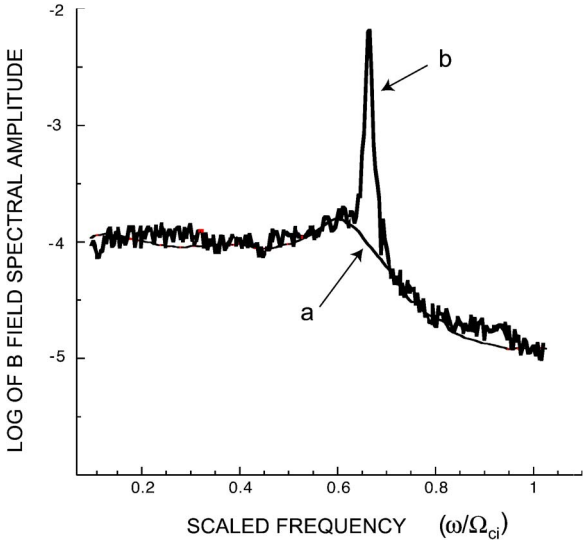

FIG. 12. Example of a maser spectrum measured in the laboratory to illustrate its similarity to predictions of differential equation model. Experimental details are given in Ref. 2. Curve (a) is the ambient noise spectrum of the laboratory resonator and curve (b) is the behavior when the operational maser threshold is exceeded.

of the confinement magnetic field. For a given resonator configuration and plasma density the frequency can be tuned by varying the field strength.

To better illustrate the similarity between the result of the differential equation model and the experimental observations, Fig. 12 displays a characteristic maser spectrum measured in the laboratory (for details Ref. 2 should be consulted). Again, curve (a) represents the noise spectrum of the laboratory resonator and curve (b) the behavior when the threshold condition is exceeded.

The effect of the gradient of the confinement magnetic field on the maser spectrum is illustrated in Fig. 13 for two values of the depth of the magnetic field modulation, $\delta=0$, 0.35. It is seen that for the uniform field configuration (i.e.,

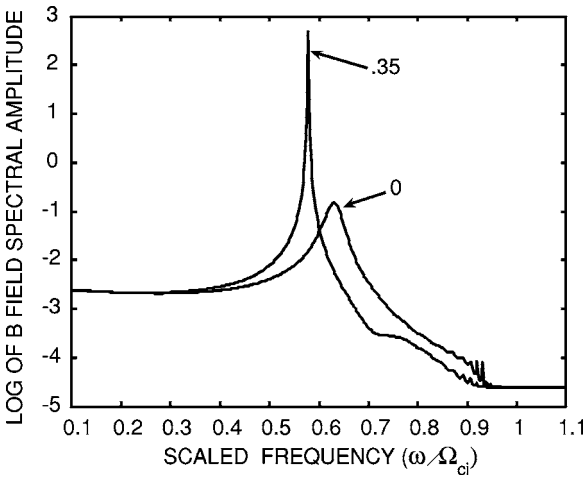

FIG. 13. Effect of the gradient of the confinement magnetic field on the maser spectrum for two values of the depth of the magnetic field modulation, $\delta=0$, 0.35. For the uniform field configuration ($\delta=0$) the maser peak is broadened and reduced in amplitude, while the spectral amplitude for $w>0.6$ is enhanced.

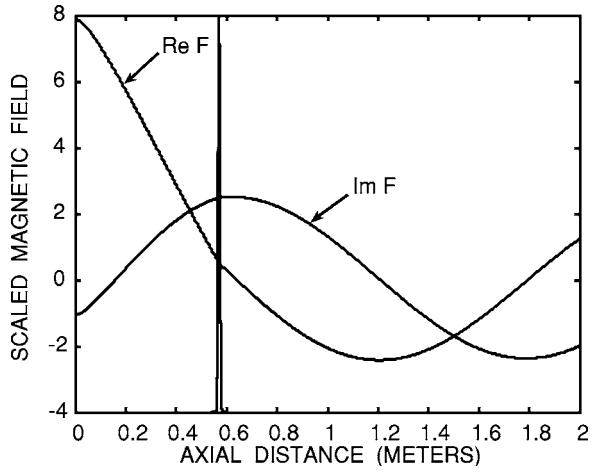

FIG. 14. Spatial dependence of the scaled magnetic field associated with the sharp maser peak of Fig. 11. The oscillating curves correspond to the real (Re F) and imaginary (Im F) parts of the maser eigenmode having scaled frequency $w=0.578$. The sharp spike centered at $z=0.57$ m indicates the location of the semitransparent grid anode.

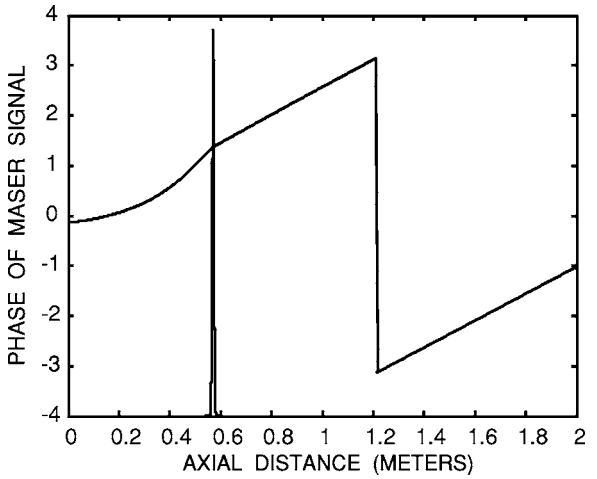

FIG. 15. Phase of the maser eigenmode displayed in Fig. 14. The sharp spike indicates the location of the grid anode. Within the resonator the eigenmode experiences a net phase difference of approximately $\pi/2$. Outside the resonator the phase undergoes multiple shifts of 2π, as is characteristic for a traveling wave.

$\delta=0$) the maser peak corresponding to curve (b) of Fig. 11 is broadened and reduced in amplitude. The frequency of the peak is increased to a scaled value of $w=0.63$. It is also seen that the spectral amplitude for $w>0.6$ is enhanced, as expected, because these modes no longer encounter a cyclotron resonance within the resonator. In the frequency interval around $w=0.9$ some small peaks appear. These correspond to higher-order resonances having small wavelength.

The spatial dependence of the scaled magnetic field associated with the sharp maser peak of Fig. 11 is displayed in Fig. 14. The two oscillating curves correspond to the real (Re F) and imaginary (Im F) parts of the maser eigenmode having scaled frequency $w=0.5783$. The sharp spike centered at $z=0.57$ m is shown to indicate the location of the semitransparent grid anode. It is seen that within the resonator region ($z<0.57$ m) the eigenmode is a partially standing signal that approximately fits one-quarter of a wavelength between the cathode ($z=0$) and the grid anode. To the right of the grid ($z>0.57$ m) the signal is a propagating shear Alfvén wave.

The phase of the maser eigenmode displayed in Fig. 14 is shown in Fig. 15. The sharp spike again indicates the location of the grid anode. It is seen that within the resonator the eigenmode experiences a net phase difference of approximately $\pi/2$. Outside the resonator the phase undergoes multiple shifts of 2π, as is characteristic for a traveling wave. Figures 14 and 15 conclusively indicate that the region defined by the cathode and the grid anode in the LAPD-U configuration acts as a quarter-wave resonator. This information permits a simple prediction for the scaled frequency of the fundamental maser mode, w_m, in terms of the operational parameters (i.e., magnetic field strength, plasma density, resonator size, and ion mass). As follows from Eq. (16) for $\xi=1$, and with no source, a dispersion relation is obtained

$$-\left(\frac{1}{w^2}-1\right)k_{II}^2+\frac{\omega_{pi}^2}{c^2}=0, \tag{29}$$

which evaluated at the resonant wave number

$$k_{II}=\frac{2\pi}{\lambda_{II}}=\frac{2\pi}{4z_g}, \tag{30}$$

yields

$$w_m=\frac{\omega_m}{\Omega_i}=\frac{s}{\sqrt{1+s^2}}, \quad s=\frac{\pi c}{2z_g\omega_{pi}}. \tag{31}$$

For the parameters leading to the maser peak represented by curve (b) in Fig. 11, Eq. (31) predicts a value $w_m=0.586$, which is remarkably close to the result obtained from the numerical solution of the differential equation.

C. Multicavity masers

Having established the properties of the maser operation corresponding to the existing configuration in the LAPD-U, it is useful to explore the features of alternative configurations consisting of a series of multiple cavities. This is a situation that can be implemented in the laboratory with relatively minor modifications and which can provide specific wave modes for various studies. The multiple-cavity environment is of interest also to magnetospheric maser studies. In that environment the variations in plasma parameters might naturally provide several layers where partial reflection occurs as an Alfvén wave propagates along the geomagnetic field.

The simplest laboratory arrangement of a multiple-cavity scenario is obtained by inserting a reflecting boundary at a certain axial position downstream from the grid anode. At the present time such a feature is readily available at the LAPD-U. A retractable conducting plate can be inserted that effectively reduces the axial extent of the plasma column to 10 m.

Figure 16 illustrates the changes in the noise spectrum caused by terminating the plasma with a good wave reflector. The smooth curve labeled "open" is essentially curve (a) of Fig. 11. It represents the spectrum associated with the resonator formed between the cathode and the grid anode located

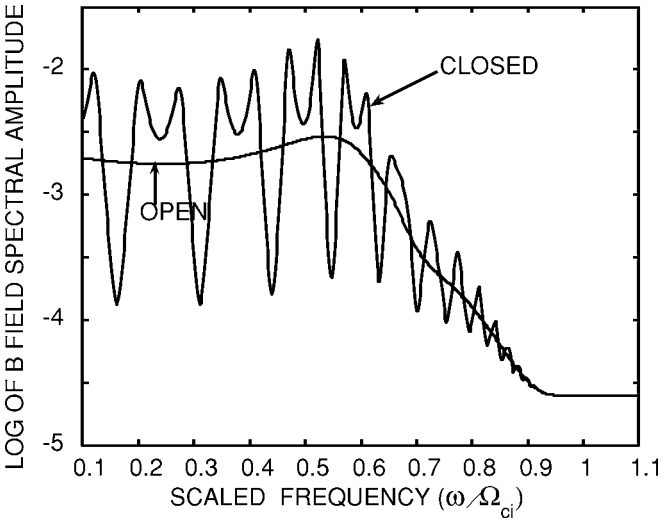

FIG. 16. Changes in the noise spectrum ($\gamma=0$) caused by terminating the plasma with a good wave reflector. The curve labeled "open" represents the spectrum with the resonator formed between the cathode and the grid anode located at $z_g=0.57$ m in an open-ended plasma. The termination of the plasma is achieved in the differential equation model by introducing a second grid with $\sigma_{s2}=100$ at $z_{g2}=10$ m and having the extent $L_{g2}=0.005$ m. The noise source is located at $z_s=0.1$ m, as in Fig. 11. The curve labeled "closed" exhibits multiple peaks and valleys that track the smooth curve. These features correspond to standing waves in the combined system composed of two leaky resonators (one short and the other long) in series. The spectrum is sampled at an axial position $z=4.95$ m.

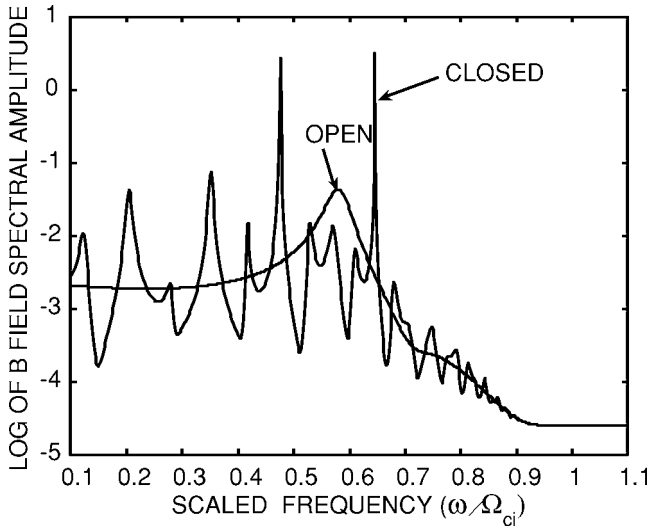

FIG. 17. Maser spectrum generated in a plasma terminated with a good reflector at $z=10$ m for an amplification region with $\gamma=-0.45$, $z_a=0$, and $L_a=1$ m. The magnetic signal is sampled at $z=4.75$ m, which is near the peak of the standing wave associated with the "open machine" maser peak occurring at $w=0.578$. For the closed machine this frequency is not amplified. Instead, two new sharp maser peaks emerge. One is at a lower frequency $w=0.476$ and the other at a higher frequency $w=0.646$.

at $z_g=0.57$ m. The termination of the plasma is achieved in the differential equation model by introducing a second grid with $\sigma_{s2}=100$ at $z_{g2}=10$ m and having extent $L_{g2}=0.005$ m. The noise source is located as in Fig. 11, namely at $z_s=0.1$ m with $L_s=0.1$ m, i.e., localized within the short resonator. The curve labeled "closed" is seen to exhibit multiple peaks and valleys that track the smooth curve. These features correspond to standing waves in the combined system composed of two leaky resonators (one short and the other long) in series. It is to be noted that the spectrum shown in Fig. 16 is sampled at an axial position $z=4.95$ m. As expected for standing waves, the relative amplitudes of the spectral peaks and valleys vary with the axial position sampled.

The dependence of the spectrum under maser action is significantly more complicated when there is feedback from a reflecting end plate. The reason is that amplification depends sensitively on the phase of the maser mode and also on the overlap between the amplification region and the spatial shape of the eigenmode, as illustrated earlier in Fig. 10. The resulting complex behavior is illustrated in Fig. 17 for an amplification region with $\gamma=-0.45$, $z_a=0$, and $L_a=1$ m. This corresponds to amplification in the neighborhood of the short resonator and negligible amplification in the large one. The magnetic signal is sampled at an axial location $z=4.75$ m, which is near the peak of the standing wave associated with the "open machine" maser peak occurring at $w=0.5783$. It is seen that for the closed machine this frequency is not amplified. Instead, two new sharp maser peaks emerge. One is at a lower frequency $w=0.476$ and the other at a higher frequency $w=0.646$. Although it is not shown, it is worth mentioning that if the amplification region extends significantly into the large resonator, it is found that the principal maser frequency is accordingly shifted to lower frequencies. Again, the amplitudes of the amplified peaks vary with axial position.

Because of the complicated spectral relationship for maser action obtained in a closed machine, care must be exercised in the interpretation of experimental results in this environment. On first impression the development of sidebands around the original maser peak can be highly suggestive of parametric coupling and/or some form of nonlinear cascade. This misleading perspective can be further enhanced under a casual examination by the presence of peaks at lower frequencies. As shown in Fig. 17, these additional peaks have values comparable to the frequency splitting between the open machine maser mode and those amplified with the end plate inserted. However, the physics responsible for such spectral features in the present study is entirely linear.

An interesting two-cavity arrangement consists of adding a second, semitransparent grid at a location corresponding to twice the distance from the cathode to the first anode grid, i.e, $z_{g2}=2z_{g1}=1.14$ m. In this case one has a series of identical resonators with partial feedback and the issue is how they interact with each other. The corresponding magnetic field spectrum sampled to the right of the second grid (at $z=2$ m) is shown in Fig. 18, which is to be compared to the single-cavity result shown in Fig. 11. The fluctuation source is located inside the first cavity at $z_s=0.1$ m with $L_s=0.2$ m. The grids have identical effective conductivity $\sigma_{s1}=\sigma_{s2}=1.1$ and width $L_{g1}=L_{g2}=0.005$ m. Curve (a) corresponds to the noise spectrum ($\gamma=0$) of the series resonators while curve (b) displays a sharp maser peak at $w=0.64$. The maser action arises when an amplification region is present with $\gamma=-0.725$, $z_a=0$, $L_a=1$ m, i.e, it extends over the two

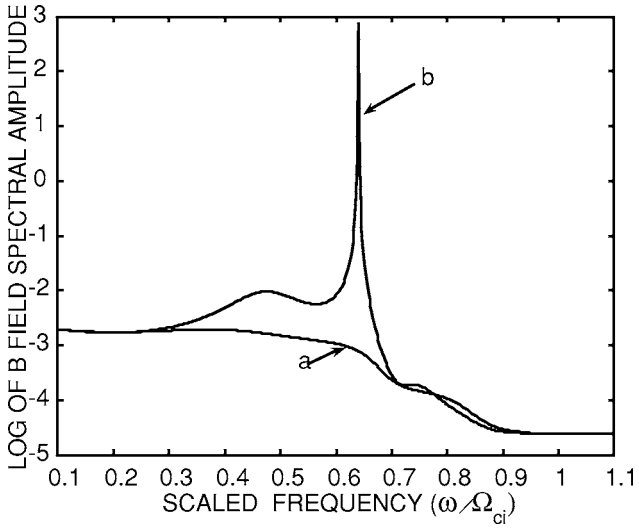

FIG. 18. Maser spectrum in a two-cavity arrangement formed by adding a second, semitransparent grid at a location corresponding to twice the distance from the cathode to the first anode grid, i.e, $z_{g2}=2z_{g1}=1.14$ m. The magnetic field spectrum is sampled at $z=2$ m and is to be compared to the single-cavity result shown in Fig. 11. The source is located inside the first cavity at $z_s=0.1$ m. The grids have identical effective conductivity $\sigma_{s1}=\sigma_{s2}=1.1$ and width $L_{g1}=L_{g2}=0.005$ m. Curve (a) corresponds to the noise spectrum ($\gamma=0$) of the series resonators, while curve (b) displays a sharp maser peak at $w=0.64$. Maser action arises when an amplification region is present with $\gamma=-0.725$, $z_a=0$, $L_a=1$ m.

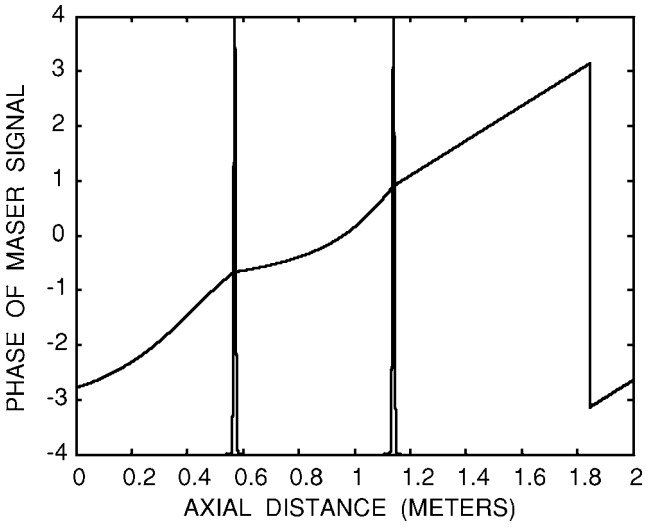

FIG. 19. Spatial dependence of the phase of the maser eigenmode for the two-cavity scenario shown in Fig. 18. The sharp spikes centered at $z=0.57$ and 1.14 m indicate the location of the semitransparent grids. The interaction between the two resonators supports a sharp maser line when the phase difference between the two grids is approximately $\pi/2$, while simultaneously the phase difference between the cathode and the anode is approximately $2\pi/3$.

cavities. It is seen that this resonator arrangement also exhibits an excellent single-mode maser operation, but it provides the added flexibility of shifting the wave frequency to higher value. Of course, the absolute scaling of the maser frequency with the strength of the confinement magnetic field still holds for this case.

The spatial dependence of the phase of the maser eigenmode for the two-grid scenario is shown in Fig. 19. It is found that the interaction between the two resonators supports a sharp maser line when the phase difference between the two grids is approximately $\pi/2$, while simultaneously the phase difference between the cathode and the anode is approximately $2\pi/3$. Under such conditions the simple relation for the maser frequency given by Eq. (28) does not hold and the power of the differential equation model comes into play.

IV. CONCLUSIONS

A useful mathematical model to describe the operation of an Alfvén wave maser in the laboratory has been developed. It is based on a continuous differential equation that includes all the necessary elements for maser action. The crucial role of semitransparent grids to define leaky resonators where the wave undergoes partial reflections is included through resistive terms in the effective potential. Unidirectional amplification of the wave is described by a consideration of balanced symmetry breaking between an imaginary part in the effective potential and a first derivative term that selects the direction of amplification. Inclusion of gradients in the confinement magnetic field allows for quenching of higher-order modes within the resonator. Each element of the model has been validated separately to correctly describe the desired effects. When all the elements of the model are activated the numerical results obtained are found to agree with the spectral characteristics and parameter scaling of an Alfvén wave maser presently in operation at the Basic Plasma Science Facility at UCLA.

The model allows for the generalization of maser action in multiple, embedded cavities. This permits the consideration of a variety of scenarios that may be useful in assessing future experiments that model various features related to fusion and space plasmas. Two examples of maser action in multiple cavities have been considered. One pertains to a machine with strong end reflections. It has been found that a complex spectrum can result that needs to be carefully assessed when interpreting the outcome of nonlinear experiments because the multitude of maser lines exhibit features that resemble parametric decays and/or wave cascades. The other scenario studied consists of two identical, leaky resonators in series. This configuration is found to exhibit excellent single-mode maser action and provides an additional selectivity of the maser frequency. The absolute value of the frequency for the single- and multicavity masers can be varied continuously by changing the confinement magnetic field.

The model has potential for investigating a variety of nonlinear effects because it is formulated for axial variations in the ambient plasma density. In principle, ponderomotive and/or heating changes of the density profile can be incorporated by coupling the model to suitable descriptions of such effects. Further refinements and extensions to nonlaboratory environments could include models of amplification regions of interest to specific applications, as well as generalizations of the effective conductivities of the semitransparent grids. For instance, they may include dependencies of the reflectiv-

ity on the transverse wave number as dictated by ionospheric calculations.

In summary, a valuable quantitative tool has been developed to explore Alfvénic interactions in the laboratory that relate to phenomena originally predicted for naturally occurring plasmas.

ACKNOWLEDGMENT

This work is sponsored by NSF Grant No. ATM-0138187.

APPENDIX: CYLINDRICAL GEOMETRY

This appendix sketches a procedure that allows a connection between the parameters that appear in the slab formulation of Sec. II and the more realistic, but considerably more involved, situation in which the plasma parameters have a radial dependence. Cylindrical geometry is assumed with coordinates (r,θ,z) with the confinement magnetic field along the z direction.

For the lowest azimuthal mode (i.e., $l=0$) the shear Alfvén wave is represented by two components of the fluctuating electric field (E_r, E_z) and one transverse magnetic field component B_θ. The cylindrical version of Eqs. (1)–(4) allows the electric field components to be eliminated from the problem and the simultaneous radial and axial behavior is governed by a single equation for B_θ,

$$\frac{\partial}{\partial z}\left\{\left(\frac{\Omega_i}{\omega_{pi}}\right)^2\left[1-\left(\frac{\omega}{\Omega_i}\right)^2\right]\frac{\partial}{\partial z}B_\theta\right\}-\frac{\partial}{\partial r}\left\{\frac{i\omega\nu_{ei}}{\omega_{pe}^2 r}\frac{\partial}{\partial r}\left(rB_\theta\right)\right\}=-\left(\frac{\omega}{c}\right)^2 B_\theta, \tag{A1}$$

in which, for simplicity, the effect of ion-neutral collisions and source terms has been left out.

The next step is to invoke a separation ansatz,

$$B_\theta(r,z)=\psi(r)B(z), \tag{A2}$$

in which it is assumed that the radial eigenfunction ψ can be obtained from some approximation (e.g., assuming the axial dependence follows the dispersion relation and then solving the remaining radial eigenvalue problem).

Proceeding to multiply Eq. (A1) with $r\psi^*$ and integrating from 0 to R (the plasma radius) yields the axial equation,

$$\frac{d}{dz}\left\{\left[\frac{\Omega_i^2}{\omega^2}-1\right]_0 p_1\frac{d}{dz}B\right\}+\frac{(\omega_{pi}^2)_0}{c^2}\times\left[1+i\left(\frac{\nu_{ei}}{\omega}\right)_0\left(\frac{c^2}{\omega_{pe}^2}\right)_0\left(\frac{p_2}{R^2}\right)\right]B=0, \tag{A3}$$

in which the zero subscript refers to the value of the quantity at the plasma center $(r=0)$. The parameters p_1, p_2 represent radial-average quantities, given by

$$p_1=\frac{\int_0^R drr\psi^* u^2\psi}{\int_0^R drr|\psi|^2(u^2)_0}, \tag{A4}$$

$$p_2=-\frac{\int_0^1 dss\psi^*(Rs)\frac{d}{ds}\left\{\frac{1}{s}\left(\frac{\nu_{ei}}{\omega_{pe}^2}\right)\frac{d}{ds}\left[s\psi(Rs)\right]\right\}}{\int_0^1 dss|\psi(Rs)|^2\left(\frac{\nu_{ei}}{\omega_{pe}^2}\right)_0}, \tag{A5}$$

where

$$u^2=\frac{\frac{\Omega_i^2}{\omega^2}-1}{\omega_{pi}^2}. \tag{A6}$$

From the structure of Eqs. (A3)–(A5) it is seen that p_1 represents an average of the perpendicular dielectric, while the quantity p_2/R^2 plays the role of the square of the perpendicular wave number $k_\perp$ appearing in Eq. (6), i.e.,

$$k_\perp^2\rightarrow\frac{p_2}{R^2}. \tag{A7}$$

[1] J. E. Maggs and G. J. Morales, Phys. Rev. Lett. **91**, 035004 (2003).
[2] J. E. Maggs, G. J. Morales, and T. A. Carter, Phys. Plasmas **12**, 013103 (2005).
[3] S. V. Polyakov, V. O. Rapoport, and V. Yu. Trakhtengerts, Fiz. Plazmy **9**, 371 (1983).
[4] P. P. Belyayev, S. V. Polyakov, and V. Yu. Trakhtengerts, Geomagn. Aeron. **24**, 2 (1984).
[5] V. Yu. Trakhtengerts and A. Ya. Feldstein, J. Geophys. Res. **96**, 19363 (1991).
[6] B. J. Thompson and R. L. Lysak, J. Geophys. Res. **101**, 5359 (1996).
[7] R. L. Lysak, J. Geophys. Res. **104**, 10017 (1999).
[8] O. A. Pokhotelov, D. Pokhotelov, A. Strelsov, V. Kruschev, and M. Parrot, J. Geophys. Res. **105**, 7737 (2000).
[9] R. L. Lysak and Y. Song, J. Geophys. Res. **107**, 1160 (2002).
[10] C. C. Chaston, J. W. Bonnell, C. W. Carlsson, J. P. McFadden, R. E. Ergun, R. J. Strangeway, and E. J. Lund, J. Geophys. Res. **109**, A04205 (2004).
[11] R. Boswell, Nature (London) **245**, 352 (2003).
[12] Y. Amagishi and M. Tanaka, Phys. Rev. Lett. **71**, 360 (1993).
[13] J. E. Maggs and G. J. Morales, Phys. Plasmas **10**, 2267 (2001).